

Article

An Efficient Bidirectional DC Circuit Breaker Capable of Regenerative Current Breaking for DC Microgrid Application

Md Mahmudul Hasan , Lo Hai Hiung, Ramani Kannan  and S. M. Sanzad Lumen 

Electrical and Electronics Engineering Department, Universiti Teknologi PETRONAS, Bandar Seri Iskandar 32610, Malaysia; lo_haihiung@utp.edu.my (L.H.H.); ramani.kannan@utp.edu.my (R.K.); s_18003309@utp.edu.my (S.M.S.L.)

* Correspondence: md_22006032@utp.edu.my

Abstract: The direct current circuit breaker (DCCB) is extensively employed in DC microgrid applications to protect the network during faults. However, numerous DC converters are combined in parallel to form a DC microgrid, which creates a large network inductance. The grid stores energy during regular operation, which repels instantaneous current breaking, and this stored energy needs to be eliminated after current breaking. Conventional topologies use different energy absorption methods to dissipate the stored energy after breaking the current. In this paper, an efficient bidirectional DC circuit breaker (EBDCCB) topology is introduced to extract and reuse this energy instead of dissipating it. The proposed topology has bidirectional power flow capability to meet the requirements of DC microgrid applications as energy storage devices are frequently utilized. Furthermore, EBDCCB shows drastically improved performance in terms of current breaking time, voltage stress, regenerated average current, and energy recovery efficiency compared to the conventional DCCB topology. The mathematical modeling and sizing of the components used in the proposed EBDCCB are elaborately analyzed, and detailed performance testing is presented along with extensive PSIM software simulation. Additionally, an experimental investigation is conducted on a laboratory-scale 48 V/1 A prototype.

Keywords: DC circuit breaker; bidirectional current breaking; DC microgrid; power system protection



Citation: Hasan, M.M.; Hiung, L.H.; Kannan, R.; Lumen, S.M.S. An Efficient Bidirectional DC Circuit Breaker Capable of Regenerative Current Breaking for DC Microgrid Application. *Electronics* **2023**, *12*, 3529. <https://doi.org/10.3390/electronics12163529>

Academic Editor: Adel M. Sharaf

Received: 18 July 2023

Revised: 8 August 2023

Accepted: 16 August 2023

Published: 21 August 2023



Copyright: © 2023 by the authors. Licensee MDPI, Basel, Switzerland. This article is an open access article distributed under the terms and conditions of the Creative Commons Attribution (CC BY) license (<https://creativecommons.org/licenses/by/4.0/>).

1. Introduction

Numerous reports have recently been published in the news media, articles, magazines, and research papers about the dramatic climate change issues around the globe. Recently, a report published with the title “Malaysia’s Extreme Weather is a Sign That Climate Change Has Arrived on Our Shores” shows the current environmental effects in Malaysia due to climate change [1]. There are different indicators for climate change, such as droughts, frequent storms, floods, and rising sea levels. The observed natural disaster issues are closely associated with global warming [2], which is caused by the excessive rates of man-made carbon dioxide emissions, resulting from the burning of fossil fuels for electricity generation and transportation systems. The carbon emission rate has been increasing rapidly, and the annual emission rate has risen from 20.5 gigatons to 33.5 gigatons within the last 30 years [3]. These problems have accelerated the growth of renewable energy sources (RES). Photovoltaic systems and wind turbines are extensively used RES, and a DC microgrid network is the best option to integrate all these RES [4–7]. It uses several voltage source converters (VSCs), such as AC/DC and DC/DC, to perform power conversion. The operation of some converters is bidirectional, whereas that of others is unidirectional. Compared to the AC grid, it has several advantages such as no frequency issues, a reliable control and conversion process, and high efficiency at integrating RES. Despite the numerous advantages of DC microgrids, ensuring adequate fault protection mechanisms poses significant challenges when compared to AC grids. This is primarily due

to the absence of naturally occurring zero crossing points, which are readily available in AC systems [8,9]. The inherent characteristics of renewable energy sources (RES)-based power systems in DC systems, such as low system impedance and higher charged capacitances, result in a significant surge in fault current during sudden fault inception, reaching magnitudes several hundred times higher than the nominal value. However, this drawback of DC microgrids can be mitigated through the utilization of various advanced fault detection and load isolation methods [10–12]. Throughout the years, DC circuit breakers have proven to be a reliable solution for interrupting the flow of current in DC systems, serving the crucial purposes of fault isolation and load switching. The DCCB should have the following features: the ability to break current in both directions, manual tripping, voltage surge protection during current breaking, galvanic isolation, low conduction loss, high reliability, a long lifespan, and energy-efficient operation [13]. Conventional DCCBs can be classified into four categories: (i) mechanical circuit breaker (MCB), (ii) solid state circuit breaker (SSCB), (iii) hybrid circuit breaker (HCB), and (iv) Z-source circuit breaker (ZCB). These four types of DCCB are different from each other in terms of current breaking technique, structure, and control mechanism. Since the early stage of development, MCBs had been used for the AC interruption in conventional power systems, but they have since been extensively applied for low-voltage DC current interruption after the emergence of the concepts of the DC grid. It uses simple mechanical switches in parallel with the other two branches to create current oscillation and energy absorption. An arc is generated due to mechanical contact separation during current interruption, which is extinguished by the MCB using different techniques [14]. The current oscillation branch is an LC resonance circuit that is used to create a forced current zero point during the current interruption, and the residual stored energy of the network inductance is dissipated as a form of heat using different types of lossy networks such as nonlinear resistance and metal-oxide varistor (MOV) after current interruption [15]. MCB offers negligible conduction loss, but a longer tripping time is required due to mechanical moving parts [16,17]. As the fault current rises very quickly in the DC microgrid, faster isolation is essential for its protection. In order to fulfill the requirements of fast response, mechanical switches are replaced with solid-state devices such as IGBT, TRIAC, Thyristors, GTO, etc., which are known as SSCB. The current interruption is done using solid-state devices, and an energy absorption part is attached in parallel to it that limits voltage surge and performs the dissipation of the stored energy of the network inductance during current breaking operation [18]. In the literature, many upgraded SSCBs are found with advanced features [19–21]. Although these have many benefits compared to the MCB, very high conduction losses occur during normal operation, and galvanic isolation makes them inappropriate for high-voltage applications. To tackle this challenge, a new solution called the Hybrid Circuit Breaker (HCB) has been introduced. The HCB combines the structural principles of both MCB and SSCB to leverage the benefits offered by both technologies. By incorporating arcless operation, rapid current interruption, minimized conduction losses, and galvanic isolation, the HCB aims to address the aforementioned issues effectively. It uses three components to perform its operation: a fast mechanical switch (FMS), semiconductor switches, and MOV. The HCB operates in a sequential manner. Upon receiving a tripping pulse, the FMS initiates the separation of contacts and simultaneously generates a turn-on pulse for the semiconductor switch (SS). As the current traverses through the FMS and reaches the predetermined arc voltage across FMS, it commutates automatically toward the threshold value of the SS. This conduction of current persists until FMS blocks the full voltage. Subsequently, FMS is turned off, causing the system voltage to rise gradually up to the breakdown voltage of the MOV due to the inherent inductance of the system. Upon reaching the MOV's breakdown voltage, it is triggered, enabling the current to flow through it and dissipate the stored energy effectively. Although the advantages compared to the aforementioned DCCB have been proven, few limitations are observed because of response times and current rating differences between FMS and SS [22,23]. Regarding the fault conditions, the contact separation of the FMS depends on the fault magnitude. The arc voltage of FMS needs to be high enough to

reach the threshold value of SS , and the arc needs to be extinguished [24]. Subsequently, a modification is made to the conventional SSCB to respond autonomously during fault without any external sensing or control device, named the ZCB. It offers several advantages such as auto-tripping, inherent coordination, fault current limiting mechanisms, etc. ZCB uses an LC network for the current interruption. During the fault, it allows a large portion of the fault current to pass through the capacitors, and the inductor prevents an abrupt current change through it when the capacitor and inductor current becomes equal, causing SCR to turn off. The LC networks create a current resonance, and diodes commute on and change the current direction. Later, the capacitor discharges across the resistor, and the circulating current from the inductor dies out through the inductor–resistor–diode circular loop. Despite the aforementioned numerous advantages, this approach cannot properly function in lower dynamic fault conditions and highly inductive networks such as DC microgrids [25].

In summary, the reviewed literature has explored various topologies, each possessing distinct characteristics and limitations. However, all the mentioned topologies utilize a conventional current-breaking technique that involves the use of lossy networks, such as impedance networks, nonlinear resistors, or snubber networks, to dissipate the stored energy post current breaking. It is worth noting that in DC microgrids, the network exhibits significant inductance, ranging from several millihenries to hundreds of millihenries, and carries current in the range of several hundred to thousands of amperes. Consequently, the network stores a substantial amount of energy, calculated as $\frac{1}{2}LI^2$. This stored energy needs to be recovered after performing the current breaking. As DC microgrids are designed for optimum utilization of energy, if there is the slightest scope of energy conservation, it should be grasped wholeheartedly for a sustainable future. Recently, a unidirectional DCCB topology has been proposed with the concept of regenerative current breaking, which ensures efficient current breaking operation along with recovery of the stored energy of the network instead of dissipating [26] as shown in Figure 1. In addition to these benefits, there are several drawbacks associated with it, including the absence of bidirectional power flow capability, high voltage stress across FMS, the large peak of regenerated current, low energy recovery efficiency, and longer tripping time. The incorporation of bidirectional power flow is recognized as a significant feature of modern DCCBs, as it aligns with the integration of energy storage systems, electric vehicles, and batteries into DC microgrids. This capability allows for efficient and flexible energy transfer in both directions, enabling the utilization and management of various energy sources and loads within the DC microgrid ecosystem. Moreover, to ensure seamless current injection during regeneration, it is essential to maintain a low peak value of the regenerated current. Failure to do so can result in voltage disturbances. Additionally, the utilization of a power diode to freewheel the energy from the load-side inductance leads to undesired energy losses.

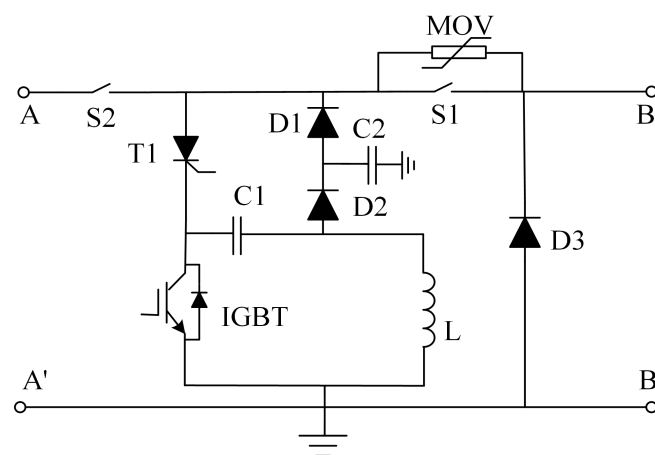


Figure 1. Conventional topology [26].

This paper introduces a much more efficient topology that addresses the issues of the DCCB proposed in [26]. Moreover, it effectively resolves the necessity of a freewheeling diode when load-side inductance is present. Furthermore, a modification is made to enable bidirectional functionality, allowing the DCCB to perform both current breaking and the injection of regenerated current on both sides. The paper includes simulation and experimental results, as presented below. The operation, modeling, and design aspects are discussed in Sections 2 and 4, while Section 5 presents the simulation and experimental findings.

2. The Proposed Efficient DC Circuit Breaker

In this section, a new topology with regenerative current breaking capability is presented. The popular regenerative braking technique is generally used in electric drives, where the mechanical energy stored in the rotor of a running motor as the rotational kinetic energy is reused during deceleration. If a running motor requires faster deceleration, the drive system forces the motor to operate as a generator by absorbing the mechanical energy from it and feeding this energy back to the source. In this way, a negative torque is generated, which decelerates the motor. There are some analogies between a running motor and an energized DC network. In a DC network, energy is stored in the network inductance and is calculated as $E_L = \frac{1}{2}LI^2$, where L is the network inductance and I is the current through it. As indicated earlier on (i.e., in the previous section), during current breaking, it is essential to remove the energy from the inductance, and this can be done by absorbing and storing that energy in a capacitor, where the energy can be expressed as $E_C = \frac{1}{2}CV^2$, where C is the capacitance and V is the voltage across it. Hence, the proposed regenerative current breaking technique introduces an impedance network (mainly, the LC network) in the current path in order to initially reduce the current to zero while storing the energy in a capacitor, and later, this stored energy is fed back to the source in a controlled manner. The construction of the proposed CB topology along with its current breaking and regeneration mechanisms is discussed in the following subsections.

2.1. Topology Introduction

The proposed efficient DC circuit breaker (EDCCB), which is developed based on the concept of hybrid CB, is introduced in Figure 2. It can be extended for high-current rating applications by adding more components. This EDCCB has three parts: (i) the main branch, (ii) the current interruption branch, and (iii) the regeneration branch. The main branch is used for the current interruption and high voltage spike reduction. It uses one FMS as a main switch for the current interruption and a low-speed (LS) switch for ensuring galvanic isolation. To limit the voltage stress during current breaking, an MOV is used in parallel to the FMS as part of the main branch. The current interruption branch consists of two thyristors (T1, T6) and LC networks (L_1, C_1). It creates a natural zero current point using a resonance circuit and store the current breaking energy in the capacitor (C_1) from source inductance (L_S). Additionally, another branch consisting of an LC network (L_2, C_1) and semiconductor switch (Q1) is used for regeneration, which is mainly a DC–DC converter. The energy of capacitor C_1 is transferred to the inductor L_2 by buck–boost mechanisms. Finally, it regenerates the current and feeds it back to the source through the diode (D1) and thyristor (T2). However, the capacitor C_2 filters the regenerated current.

$$T_{trip} = \frac{1}{\sqrt{\omega_r^2 - \gamma^2}} \left(\frac{\pi}{2} + \tan^{-1} \frac{Y}{X} \right) + T_{OFF} \tag{4}$$

while $i(t)$ crosses zero, C_1 becomes fully charged.

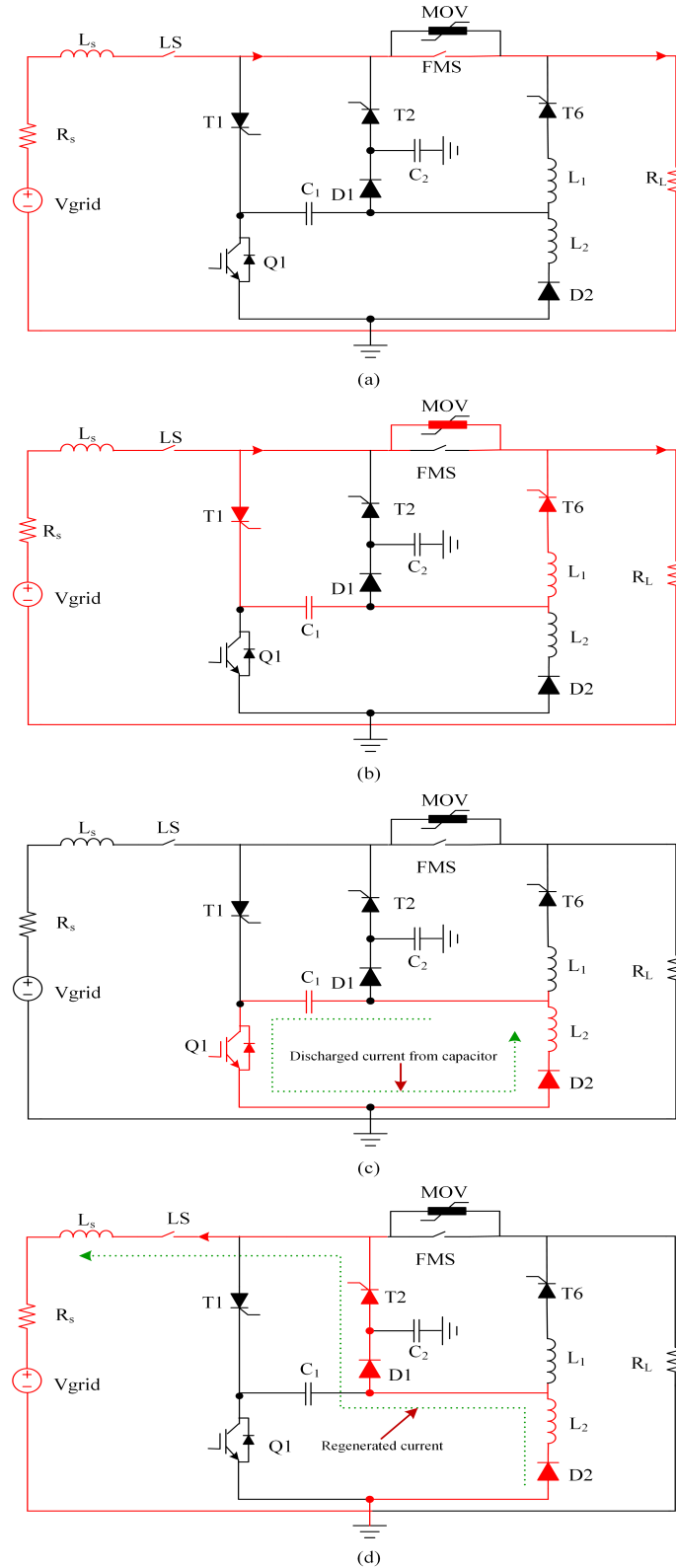


Figure 3. DCCB operation for (a) Normal current conduction mode (b) current interruption mode (c) regeneration mode (d) Current feedback mode.

2.3. Regeneration Process

During the process of regeneration, the energy stored in a charged capacitor is transferred back to the source using two modes, regeneration and current feedback, as illustrated in Figure 3c,d, respectively. These modes resemble the concept of a buck–boost converter, as depicted in Figure 4. In the regeneration process, a charged capacitor (C_1) serves as the input voltage source. It discharges through the inductor, which subsequently delivers the stored current to the grid via the series RL circuit. The average current flowing through the inductor can be expressed as follows:

$$I_{L2(\text{avg})} = \frac{1}{T_s} \int_0^{T_s} i_{L_2}(t) dt \tag{5}$$

The buck–boost mechanism operates in two distinct states: inductor charging (when the switch is turned on) and inductor discharging (when the switch is turned off) as shown in Figure 4b,c. The complete cycle of operation takes a total time of T_s . The switch remains in the on-state from 0 to $\delta \cdot T_s$ and then in the off-state from $\delta \cdot T_s$ to T_s . During the inductor charging state, the inductor is connected to the input voltage (V_{C1}) sourced from the charged capacitor. The average current flowing through the inductor ($i_{L_2}(t)$) can be mathematically represented as

$$i_{L_2}(t) = \frac{1}{L_2} \int_0^t V_{C1}(t') dt' \tag{6}$$

By integrating Equation (6) over the on-time interval $[0, \delta \cdot T_s]$,

$$\int_0^{\delta \cdot T_s} i_{L_2}(t) dt = \frac{1}{L_2} \int_0^{\delta \cdot T_s} \int_0^t V_{C1}(t') dt' dt \tag{7}$$

During the off-time, the output voltage (V_{out}) is applied to the grid network, and the inductor supplies current to the grid. The rate of change of the inductor current can be expressed as

$$\frac{di_{L_2}(t)}{dt} = \frac{V_{\text{out}}(t) - V_S(t)}{L_2} \tag{8}$$

where $V_S(t)$ represents the voltage across the grid, considering its series resistance and inductance. Integrating Equation (8) with respect to time,

$$i_{L_2}(t) = i_{L_2}(\delta \cdot T_s) + \frac{1}{L_2} \int_{\delta \cdot T_s}^t (V_{\text{out}}(t') - V_S(t')) dt' \tag{9}$$

where $i_{L_2}(\delta \cdot T_s)$ is the inductor current at the end of the on-time. However, to regulate this discharging current, the IGBT is turned on by a Pulse Width Modulation (PWM) control signal, and each time the IGBT turns off during the PWM switching interval, the inductor current is forced to flow through the diodes (D1 and T2) towards the source as shown in Figure 3d. By substituting the expression for $i_{L_2}(t)$ from Equation (9), the integral for the average inductor current becomes

$$I_{L2(\text{avg})} = \frac{1}{T_s} \left(\int_0^{\delta \cdot T_s} \int_0^t V_{C1}(t') dt' dt \right) + \frac{1}{T_s} \int_{\delta \cdot T_s}^{T_s} \left(i_{L_2}(\delta \cdot T_s) + \frac{1}{L_2} \int_{\delta \cdot T_s}^t (V_{\text{out}}(t') - V_S(t')) dt' \right) dt \tag{10}$$

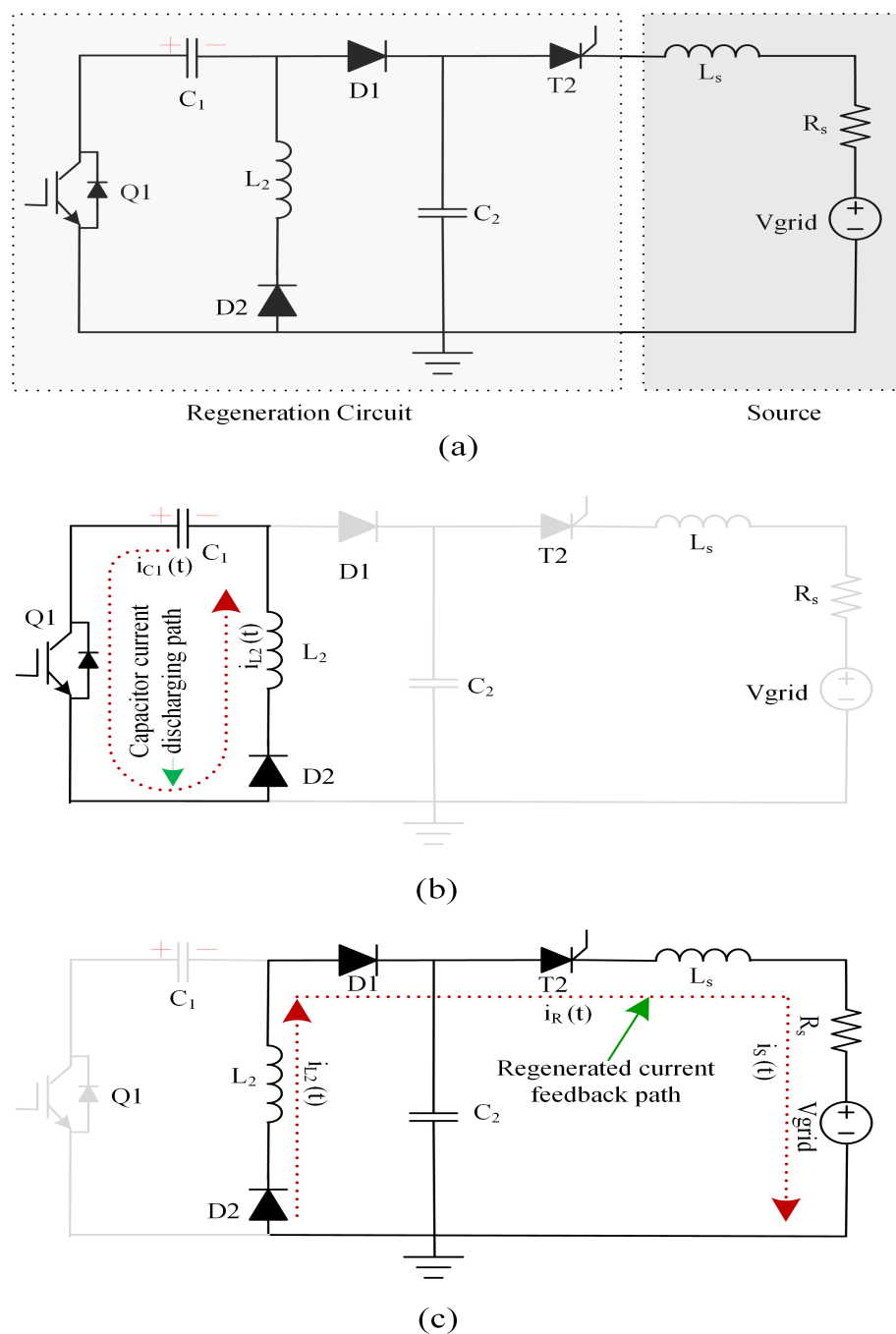


Figure 4. (a) Regeneration equivalent circuit (b) inductor charging state (c) inductor discharging state.

After simplifying the Equation,

$$\begin{aligned}
 I_{L2(\text{avg})} = & \frac{1}{T_s} \left(\int_0^{\delta \cdot T_s} \int_0^t V_{C1}(t') dt' dt \right) + \frac{1}{T_s} \left(\int_{\delta \cdot T_s}^{T_s} i_L(\delta \cdot T_s) dt \right) + \\
 & \frac{1}{T_s} \left(\int_{\delta \cdot T_s}^{T_s} \frac{1}{L_2} \int_{\delta \cdot T_s}^t (V_{\text{out}}(t') - V_S(t')) dt' dt \right)
 \end{aligned} \tag{11}$$

The term from Equation (11), $\int_{\delta \cdot T_s}^{T_s} \frac{1}{L_2} \int_{\delta \cdot T_s}^t (V_{\text{out}}(t') - V_S(t')) dt' dt$, can be rewritten as follows:

$$\int_{\delta \cdot T_s}^{T_s} \frac{1}{L_2} \int_{\delta \cdot T_s}^t (V_{\text{out}}(t') - V_S(t')) dt' dt = \frac{1}{L_2} \int_{\delta \cdot T_s}^{T_s} \left(\int_{\delta \cdot T_s}^t (V_{\text{out}}(t') - V_S(t')) dt' \right) dt \tag{12}$$

Using the properties of definite integrals, the inner integral can be rewritten as

$$\int_{\delta \cdot T_s}^t (V_{out}(t') - V_S(t')) dt' = \int_{\delta \cdot T_s}^{T_s} (V_{out}(t') - V_S(t')) dt' - \int_t^{T_s} (V_{out}(t') - V_S(t')) dt' \quad (13)$$

Substituting this back into Equation (12), then

$$\int_{\delta \cdot T_s}^{T_s} \frac{1}{L_2} \int_{\delta \cdot T_s}^t (V_{out}(t') - V_S(t')) dt' dt = \frac{1}{L_2} \int_{\delta \cdot T_s}^{T_s} \left(\int_{\delta \cdot T_s}^t (V_{out}(t') - V_S(t')) dt' \right) dt - \frac{1}{L_2} \int_{\delta \cdot T_s}^{T_s} \left(\int_t^{T_s} (V_{out}(t') - V_S(t')) dt' \right) dt \quad (14)$$

This can be simplified further by evaluating the integrals:

$$\int_{\delta \cdot T_s}^{T_s} \left(\int_{\delta \cdot T_s}^t (V_{out}(t') - V_S(t')) dt' \right) dt = \int_{\delta \cdot T_s}^{T_s} ([V_{out}(t') - V_S(t')] \cdot (t - \delta \cdot T_s)) dt = [V_{out}(t') - V_S(t')] \cdot \left(\frac{1}{2} (t - \delta \cdot T_s)^2 \Big|_{\delta \cdot T_s}^{T_s} \right) \quad (15)$$

and

$$\int_{\delta \cdot T_s}^{T_s} \left(\int_t^{T_s} (V_{out}(t') - V_S(t')) dt' \right) dt = \int_{\delta \cdot T_s}^{T_s} ([V_{out}(t') - V_S(t')] \cdot (T_s - t)) dt = [V_{out}(t') - V_S(t')] \cdot \left(\frac{1}{2} (T_s - t)^2 \Big|_{\delta \cdot T_s}^{T_s} \right) \quad (16)$$

Substituting the results from Equations (15) and (16) back into Equation (11), and after simplifying further,

$$I_{L2(avg)} = \frac{1}{T_s} \left(A + \frac{1}{2 \cdot L_2} B \right) = I_{r(avg)} = I_{s(avg)} \quad (17)$$

where, $A = \int_0^{\delta \cdot T_s} \int_0^t V_{C1}(t') dt' dt + \int_{\delta \cdot T_s}^{T_s} i_{L2}(\delta \cdot T_s) dt$ and

$$B = \left[(V_{out}(t') - V_S(t')) \cdot ((t - \delta \cdot T_s)^2 - (T_s - t)^2) \Big|_{\delta \cdot T_s}^{T_s} \right]$$

At this instant, the dynamics of the current $i_{L_2}(t)$ can be represented by (9), where $i_{L_2}(\delta \cdot T_s)$ is the initial inductor current each time the IGBT (Q1) turns off. The capacitor C_2 smooths out the inductor current. This phenomenon of feeding current back to the source is defined as regeneration in this paper. This regenerated current can recharge the battery if the battery was used as a source, or it can be fed to other loads connected to the source. As soon as the capacitor is completely discharged, the PWM signal stops turning off the IGBT, and the regenerated current decays to zero. Once the regenerated current becomes zero, switch LS turns off and resets the breaker.

2.4. Theoretical Analysis and Design Considerations

The design process of the proposed DCCB relies on the network parameters, including the maximum fault current (I_{MAX}), maximum fault clearing time (T_{MAX}), and maximum allowable voltage (V_{MAX}). These parameters are crucial in the design of the breaker. To determine the maximum capacitor voltage (V_{C1}), the following calculation must be performed. During Mode-2 operation, capacitor C_1 primarily accumulates energy from the source-side inductance, but a portion of the energy also originates from the source. Simultaneously, due to turn-off delay, a fraction of energy (E_{LOAD}) is lost to the load. To obtain the stored energy by capacitor (E_{C1}), the leaked energy from the load (E_{LOAD}) needs

to be subtracted from the accumulated energy released by the source side inductance (E_s). This can be expressed as follows:

$$E_{C1} \approx E_s - E_{LOAD} \tag{18}$$

$$\frac{1}{2} C_1 V_{C1}^2 \approx \frac{1}{2} L_s I_o^2 + (V_{DC} I_{S(avg)} - I_{S(avg)}^2 R') T_{trip} - (V_{DC} I_o - I_o^2 R_s) T_{OFF} \tag{19}$$

where E_s is the energy stored in the source inductance (L_s) during normal operation and $I_{S(avg)}$ is the average source current during tripping intervals. Using Equation (20), the average current can be calculated as follows:

$$I_{S(avg)} = \frac{I_o T_{OFF} + \int_0^{(T_{trip}-T_{OFF})} I_s(t) dt}{T_{trip}} \tag{20}$$

$$V_{C1} \approx \frac{1}{\sqrt{C_1}} \{L_s I_o^2 + 2 (V_{DC} I_{S(avg)} - I_{S(avg)}^2 R') T_{trip} - 2 (V_{DC} I_o - I_o^2 R_s) T_{OFF}\}^{\frac{1}{2}} < V_{MAX} \tag{21}$$

As this design is system-specific, this conditions $V_{C1} < V_{MAX}$ and $T_{trip} < T_{MAX}$ need to be applied in the Equations (4) and (21). Using these two equations, the values of C_1 and L_1 can be calculated.

During the process of regeneration, the DCCB operates akin to a buck–boost converter, where capacitor C_1 acts as a continuous current conduction mode (CCM) source, facilitating the smooth regeneration of current through inductor L_2 . The frequency requirement for the PWM signal can be determined using Equations (22) and (23), where δ is the duty cycle, which is calculated using manual tuning, ΔV_{C2} is the voltage deviation, and ΔI_{L2} is the ripple current.

$$C_2 = \frac{I_{r(avg)} \delta}{\Delta V_{C2} f} \tag{22}$$

$$L_2 = \frac{V_{C1} \delta}{\Delta I_{L2} f} \tag{23}$$

2.5. Performance Parameters Calculation

In order to assess the performance of the proposed EBDCCB, several parameters are taken into consideration, including the current breaking time, peak and average regenerated current, voltage stress, and energy recovery efficiency. The current breaking time and voltage stress can be calculated using Equations (4) and (21). However, if the regeneration time is T_R and regenerated current $i_R(t)$, then the average regenerated current can be calculated using Equation (24).

$$I_{r(avg)} = \frac{\int_0^{T_R} i_R(t) dt}{T_R} = \frac{1}{T_s} \left(A + \frac{1}{2 \cdot L_2} B \right) \tag{24}$$

The regenerated energy refers to the cumulative energy that is recovered and fed back into the source through the regeneration branch. Its calculation can be achieved using Equation (25). Furthermore, the energy recovery efficiency serves as a crucial performance metric representing the ratio of recovered energy to the total recoverable energy, as indicated in Equation (26).

$$E_r = (V_{grid} I_{r(avg)} - I_{r(avg)}^2 R_s) T_R \tag{25}$$

It is to be noted that E_{LOAD} cannot be recovered as it is dissipated during the current breaking process at the load.

$$\eta = \frac{E_r}{E_s - E_{LOAD}} 100\% \tag{26}$$

3. Modified Efficient Bidirectional DC Circuit Breaker

In DC microgrids, bidirectional power flow is often desired, especially with the growing integration of energy storage systems. While the proposed unidirectional DCCB offers arc-less fast current breaking, it lacks the ability to facilitate bidirectional power flow due to the utilization of unidirectional power electronic switches. Consequently, a suitable modification is necessary to adapt the unidirectional topology for bidirectional systems such as DC microgrids. The modified topology is depicted in Figure 5. In the modified topology, four additional thyristors are introduced in an anti-series configuration, alongside T1, T2, and T6. The operation of this modified topology is symmetrical, as illustrated in Figures 6 and 7. During each operation, two pairs of thyristors, namely (T1, T6) and (T4, T3), conduct simultaneously. The LC network and regeneration branch remain unchanged and are utilized for both forward and reverse operations. Ultimately, the regenerated current is fed back to the sources through either T2 or T5. It is important to note that the mathematical model and equations remain the same as those for the unidirectional topology.

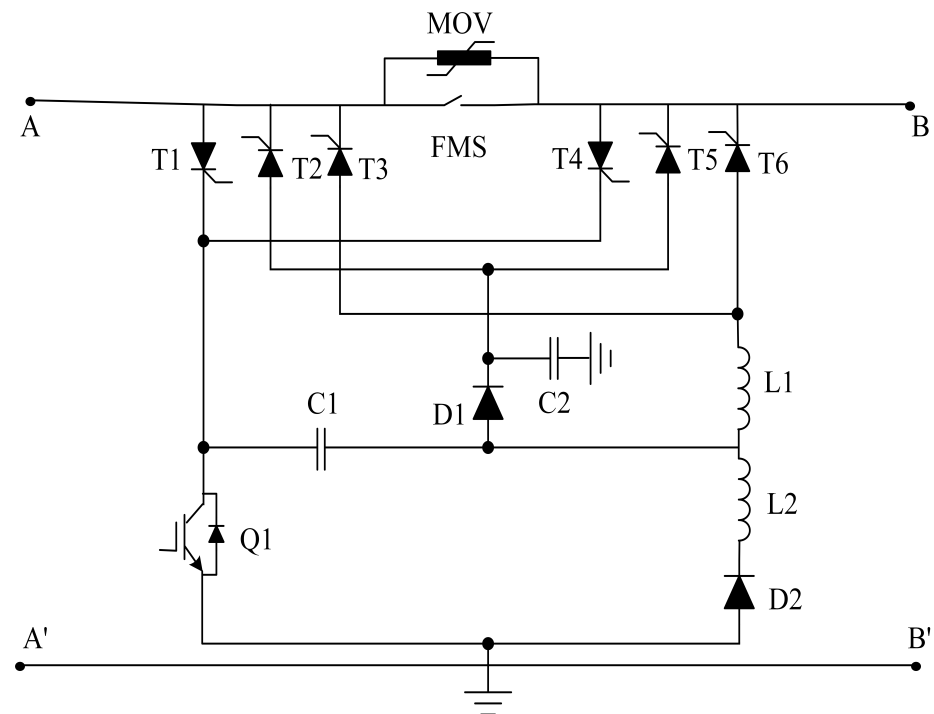


Figure 5. Modified efficient bidirectional DC circuit breaker topology (EBDCCB).

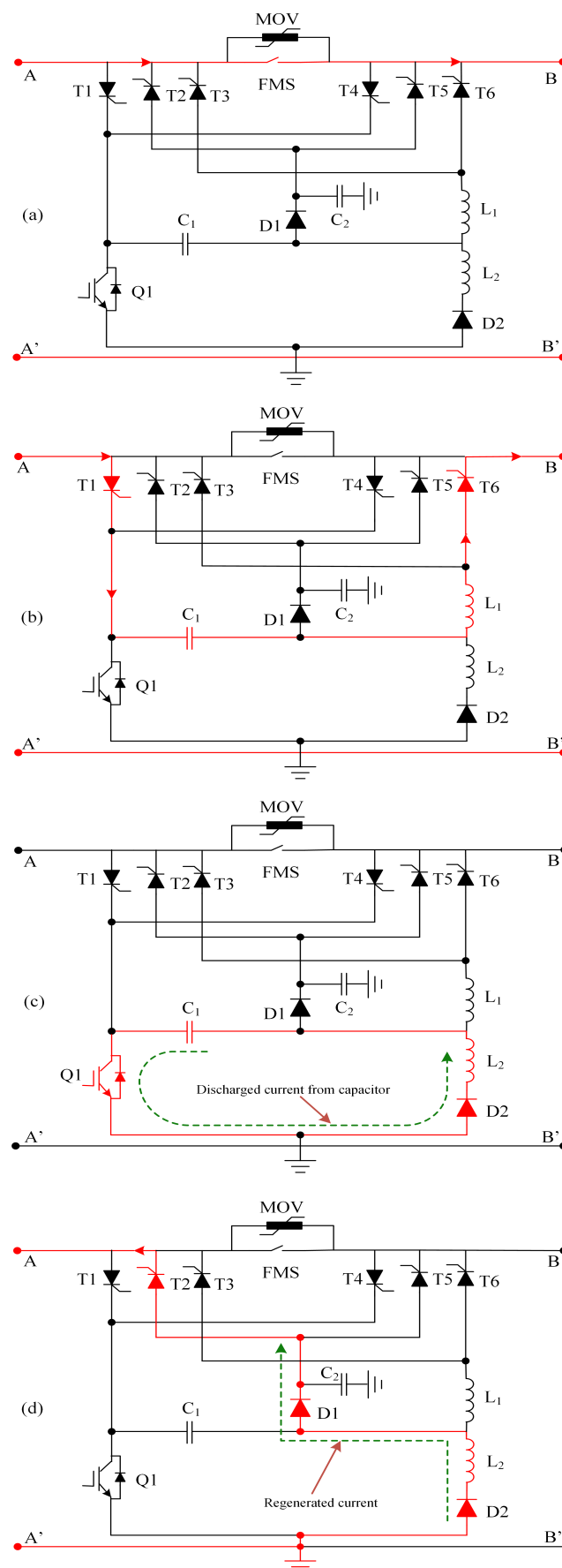


Figure 6. Mode of operation for forward conduction (a) normal operation (b) current interruption (c) current regeneration (d) current feedback.

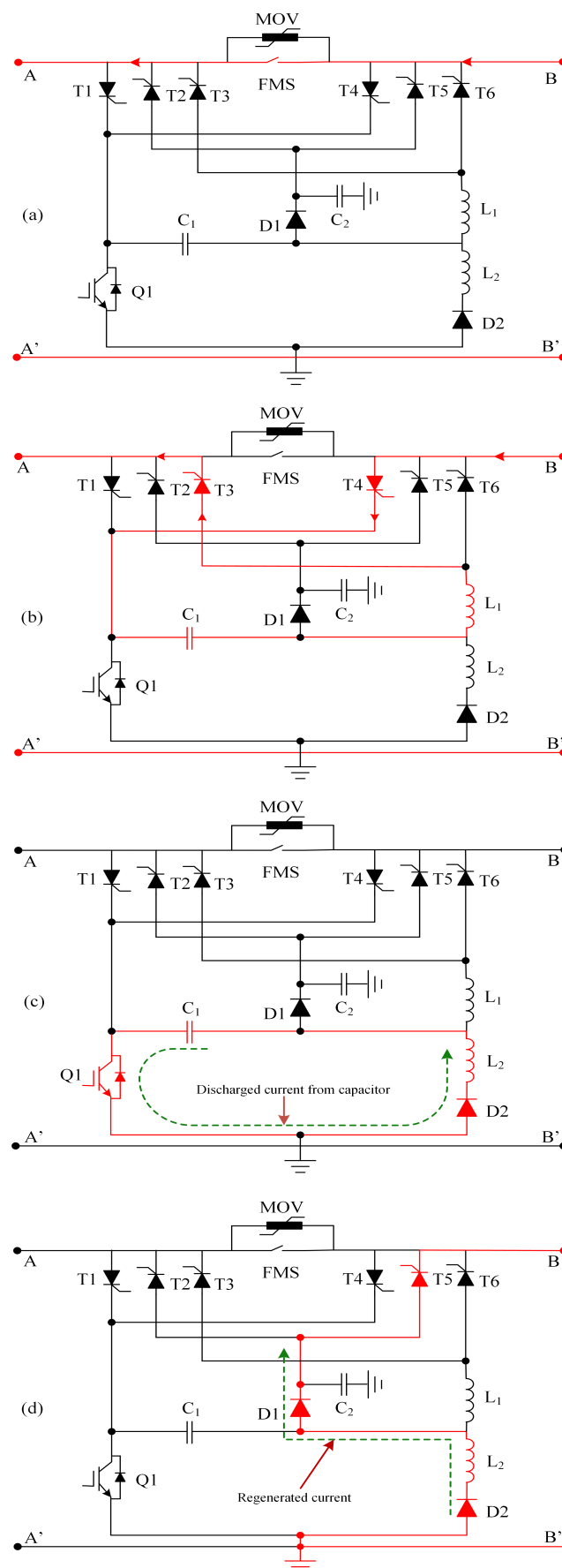


Figure 7. Mode of operation for reverse conduction (a) normal condition (b) current interruption (c) current regeneration (d) current feedback.

4. Verification

The proposed scheme has undergone validation through both simulations using PSIM software and experimentation using a dedicated setup. The outcomes of the simulations, experimental measurements, and a comparative analysis are meticulously presented in the subsequent subsection to provide a comprehensive evaluation of the proposed scheme.

4.1. Simulation Results

In this simulation, the practical components, such as IGBTs, diodes, and thyristors, are modeled with the inclusion of dynamic resistance, forward voltage drop, latching current, and other relevant characteristics. The dynamic resistance of 0.5 ohms is considered for the diodes and IGBTs. The simulation parameters are outlined in Table 1. This section focuses on presenting the outcomes obtained from the proposed topology. The runtime for the proposed EBDCCB is set to 2 s. Upon initiation, the current rises rapidly to its nominal value of 400 A. Subsequently, upon triggering the tripping pulses, the load current exhibits a swift reduction to zero, while the source current takes approximately 44.52 ms to reach zero, thus completing the current breaking operation, as depicted in Figure 8b. The duration required to decrease the load current to zero from the initiation of the tripping pulses is considered the load current breaking time, which manifests a rapid approach to zero. The current regeneration will immediately start after the source current breaking. Notably, the regenerated current attains a peak value of 157.5 A. Nevertheless, the instantaneous current breaking gives rise to high voltage spikes due to the presence of highly inductive networks. To mitigate these effects, the implementation of an MOV is recommended. During the regeneration phase, a slight voltage disturbance is observed, as demonstrated in Figure 8a, which also exhibits the source voltage, voltage stress across the FMS, and capacitor voltage. As the energy is fully transferred back to the source, the capacitor voltage gradually diminishes to zero. Figure 9 illustrates the behavior of the capacitor and inductor currents during the current breaking process. The adoption of a high switching frequency facilitates fast regeneration of the capacitor and inductor currents. To demonstrate the current breaking and regeneration capabilities, a comparative analysis of the source and load conditions in terms of voltage and current is provided in Figure 8. Additionally, the control signals employed for the proposed topology are presented in Figure 9. It is important to note that the presented results are specific to one direction only, as the inherent symmetry of the system ensures that the results would be identical for the reverse current breaking scenario as shown in Figure 10 with control signal as shown in Figure 11. This is due to the consistent parameters of the network. The comparative evaluation of performance parameters is presented in Table 2. The proposed topology, along with its associated control mechanism, showcases substantial improvements over the conventional topology and its corresponding control techniques. The performance indicators obtained from the PSIM simulation convincingly validate the efficacy of the proposed concept.

Table 1. Parameters for simulation and experimentation.

Parameter	For Simulation	For Experimentation
DC voltage (V_{dc})	400 V	48 V
Source inductance (L_s)	200 mH	2.6 H
Source resistance (R_s)	0.1 Ω	20.7 Ω
Load resistance (R_L)	0.9 Ω	27.3 Ω
Load current ($I_{LOAD} \equiv I_S$)	400 A	1 A
Maximum tripping time (T_{max})	50 ms	50 ms
Maximum system voltage (V_{max})	5000 V	300 V
Capacitance (C_1)	2000 μ F	50 μ F
Capacitance (C_2)	200 μ F	25 μ F
Inductance (L_1)	5 mH	650 mH
Inductance (L_2)	20 mH	650 mH
MOV rating	5000 V	271 V
S1 operating speed (T_{ON}/T_{OFF})	15 ms/15 ms	20 ms/20 ms

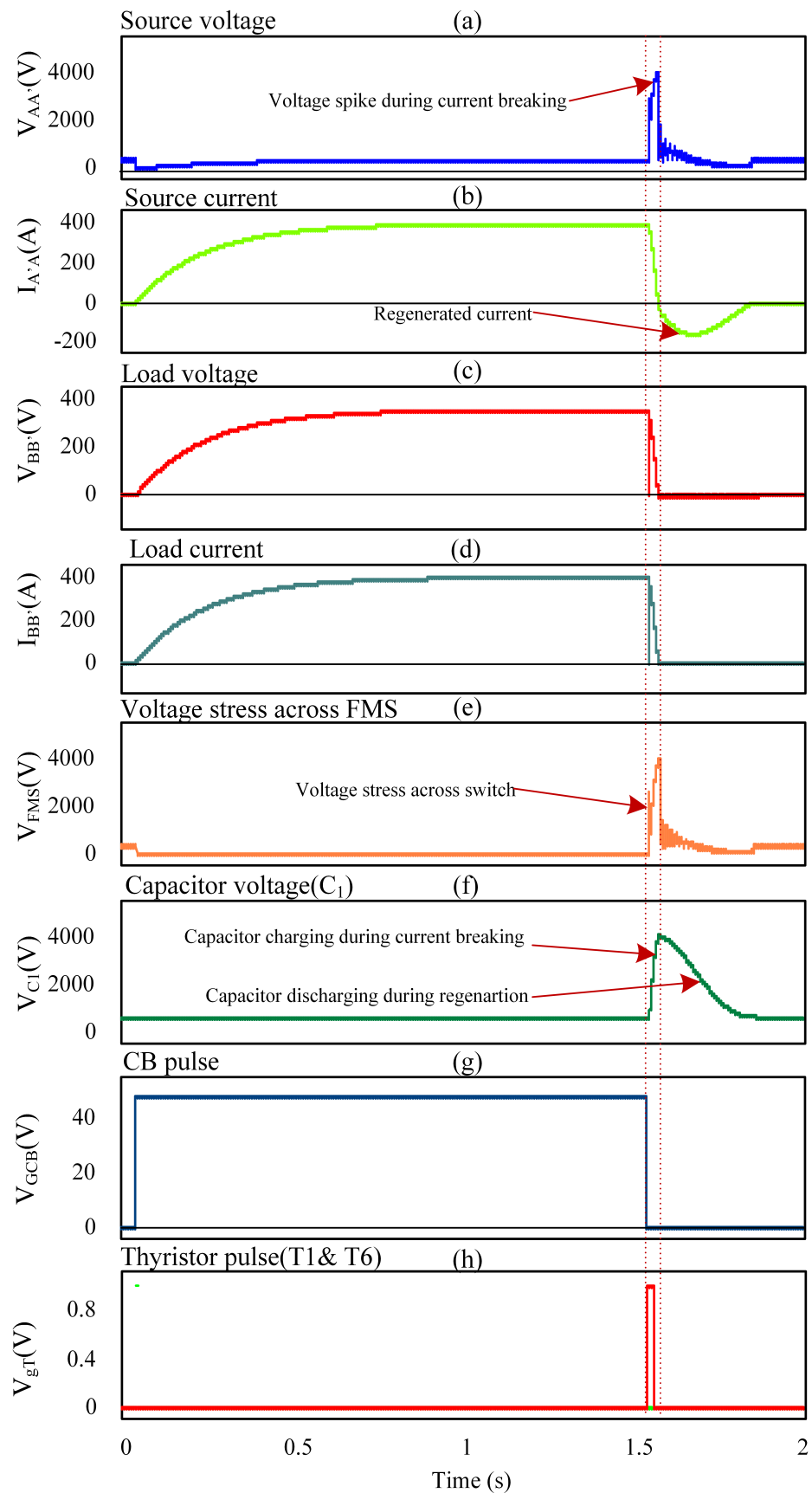


Figure 8. Simulation response for forward power flow (a) source voltage, (b) source current (c) load voltage (d) load current (e) voltage stress across the FMS (f) capacitor voltage (g) CB pulse (h) thyristor pulse (T1 and T6).

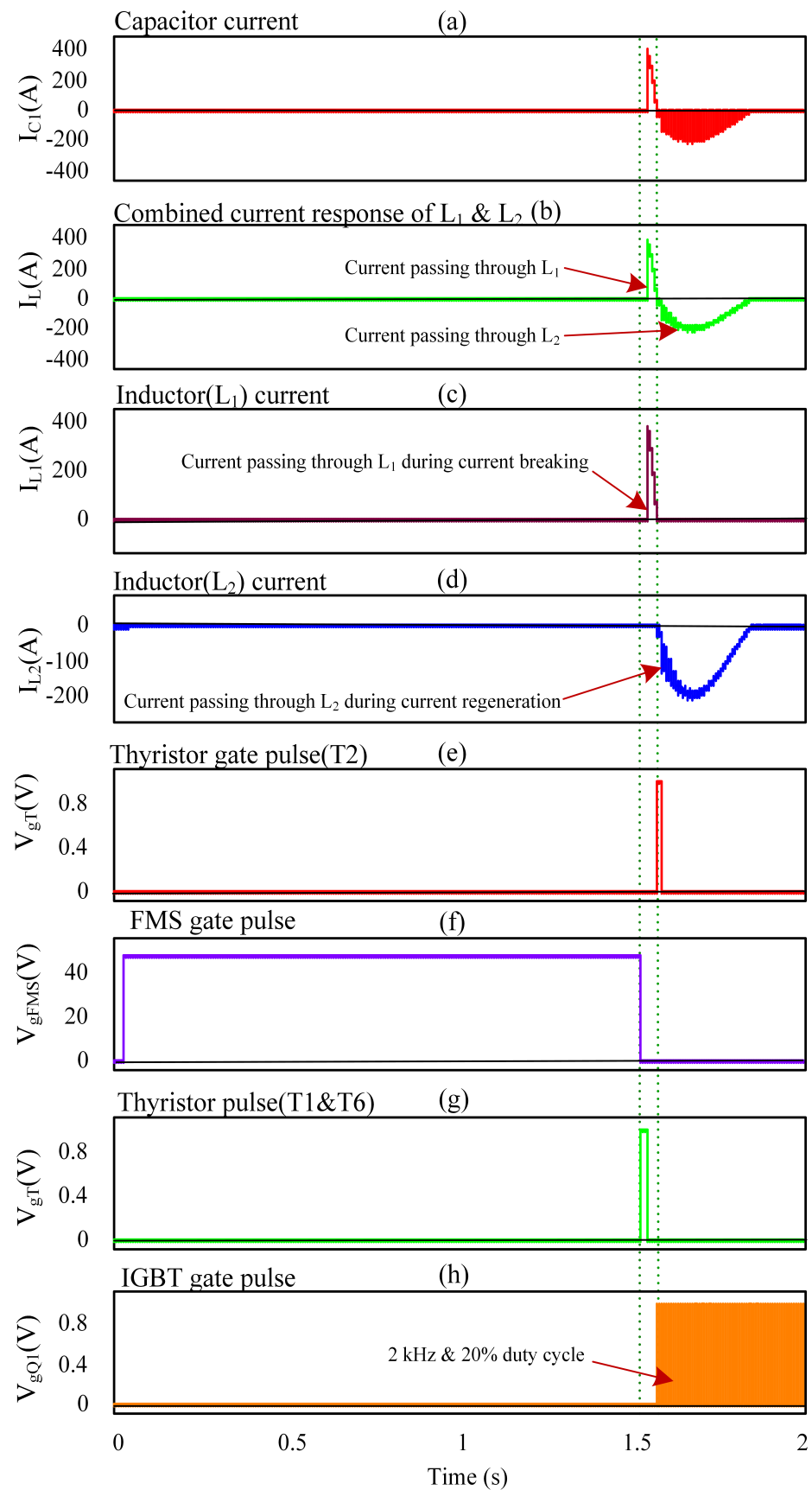


Figure 9. Simulation response for forward power flow (a) capacitor current (b) combined current through both inductors (c) current response through L_1 (d) current through L_2 (e) thyristor (T2) gate pulse (f) FMS gate pulse (g) thyristor pulses (T1 and T6) (h) IGBT gate pulse.

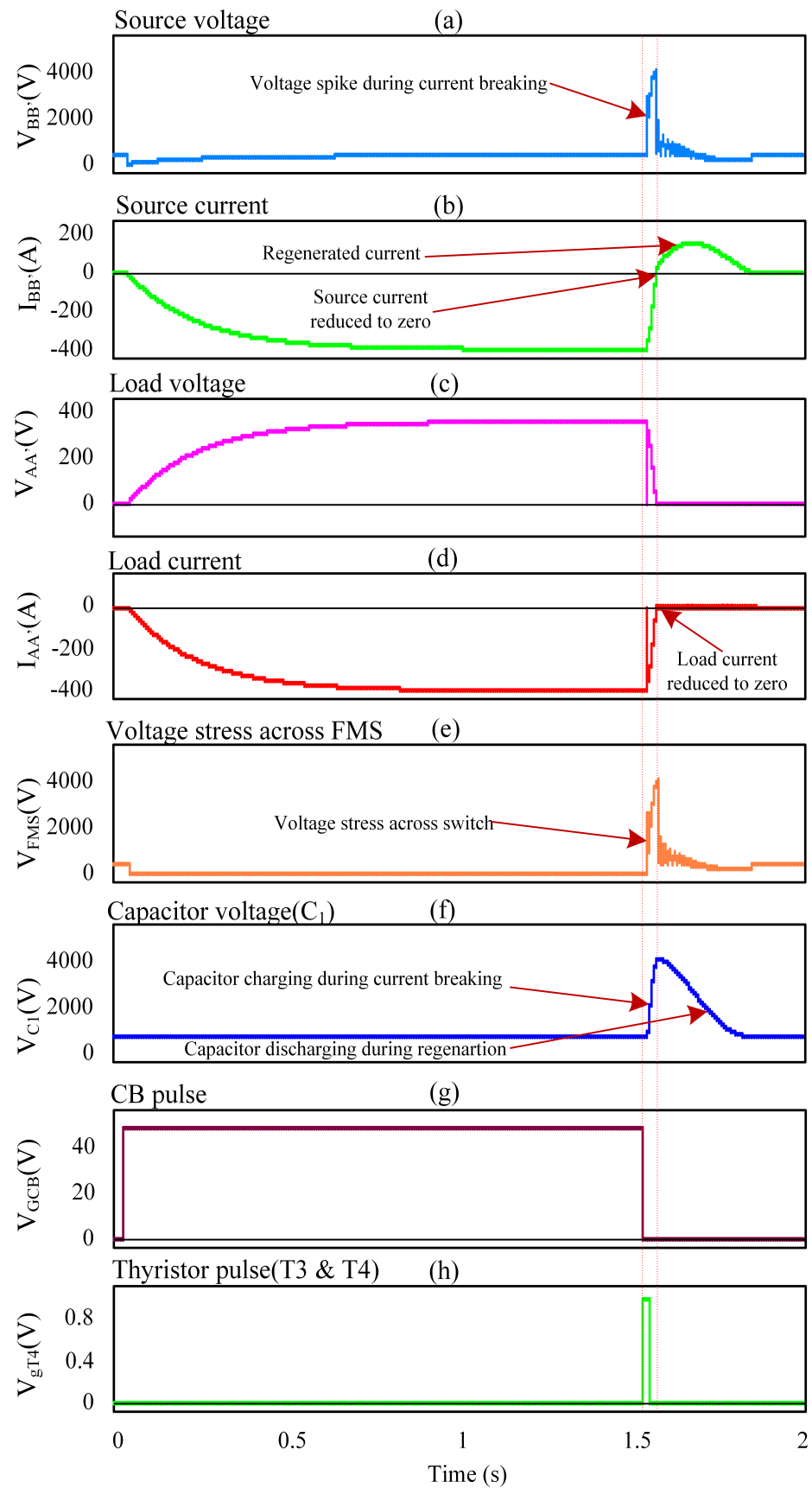


Figure 10. Simulation response of reverse power flow for (a) source voltage, (b) source current (c) load voltage (d) load current (e) voltage stress across the mechanical switch (f) capacitor voltage (g) CB pulse (h) thyristor pulse (T3 and T4).

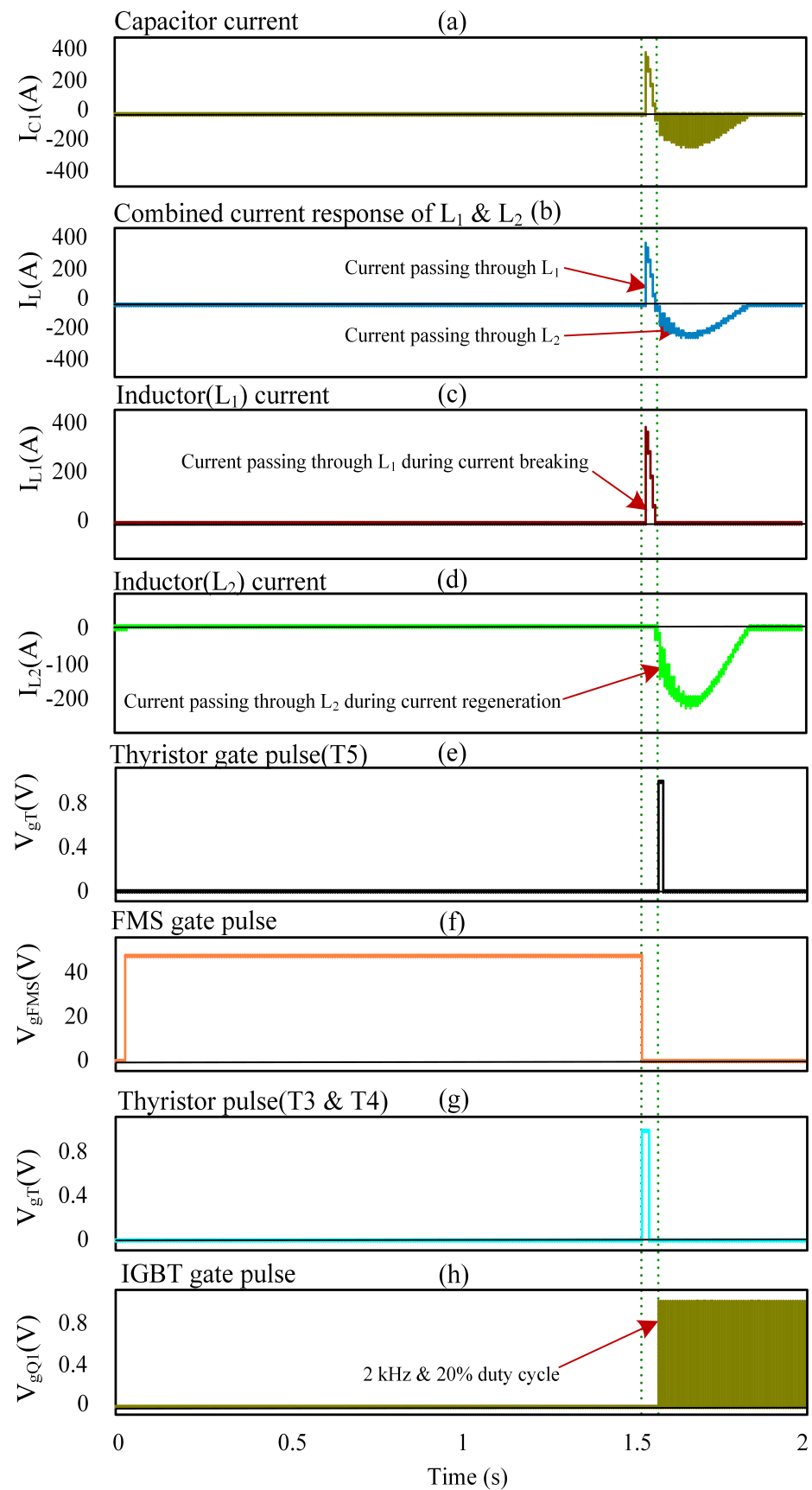


Figure 11. Simulation results of reverse power flow for (a) capacitor current (b) combined current through both inductors (c) current response through L_1 (d) current through L_2 (e) thyristor (T2) gate pulse (f) FMS gate pulse (g) thyristor pulses (T1 and T6) (h) IGBT gate pulse.

Table 2. Performance comparisons.

Performance Indicator	MCB	SSCB	ZCB	HCB	Conventional [26]	Proposed
Current breaking time (ms)	48.11	17.33	*	32.56	45.85	44.52
Conduction loss (kW)	0	16.55	1.15	0	0	0
Voltage stress (kV)	5.01	5.01	*	5.01	4.27	4.02
Regenerated current (A)	0	0	0	0	−120.88 (Average)/ −188.16 (Peak)	−100.7 (Average)/ −157.5 (Peak)
Regenerated power (kW)	0	0	0	0	−50.80 (Average)/ −116.15 (Peak)	−41.558 (Average)/ −112.7 (Peak)
Provision of galvanic isolation	Yes	No	No	Yes	Yes	Yes
Energy recovery efficiency (%)	0	0	0	0	68.24	67.26
Bidirectional current breaking	Yes	Yes	Yes	Yes	No	Yes
False tripping	No	No	Yes	No	No	No

* Tripping failure occurs in highly inductive networks, necessitating the use of higher values for the circuit breaker (CB) parameters.

4.2. Comparative Analysis

The proposed EBDCCB is simulated through PSIM software. At the same time, to compare with other topologies, PSIM simulation is used with the same network parameters. The performance comparisons are shown in Table 2. To compare the performance, five conventional topologies—MCB, SSCB, ZCB, HCB, conventional [26]—and the proposed approach are chosen. Performance parameters such as current breaking time, voltage stress, on-state loss, energy recovery efficiency, bidirectional power flow, components count, and galvanic isolation are considered as evaluation criteria. In the simulation, the conduction loss is found to be zero; however, in practical application, the conduction loss for the proposed topology will be extremely minimal due to the implementation of a mechanical switch. Table 2 indicates the superiority of the proposed DCCB compared with conventional topology. The current breaking time and voltage stress of the proposed topology are improved compared to the conventional topologies.

4.3. Experimental Validation

The performance of the proposed efficient bidirectional DC circuit breaker topology was evaluated in the laboratory on a 48 V/1 A prototype as shown in Figure 12. The lab-volt instruments are used as breaker elements and networks. The system specifications and breaker parameters are given in Table 1.

4.3.1. Experimental Setup

The proposed topology utilizes semiconductor switches and passive components as breaker elements. Specifically, it incorporates an IGBT module (Lab volt 8837) where each IGBT has a maximum voltage blocking capacity of 690 V, a maximum current of 1.5 A, and a forward dynamic resistance of 0.35 Ω . The EBDCCB also employs thyristors from the thyristor module (lab volt 8841) with a maximum voltage-blocking capacity of 1200 V. Additionally, a lab-volt power diode module with a reverse voltage blocking up to 1200 V is utilized. An FMS with a maximum tolerance capacity of 500 V and 3 A is employed to perform current braking. Its turn-on and turn-off times are approximately 15 ms. During the current interruption, an MOV with ratings of 271 V is deployed to suppress over-voltage across the switch. Moreover, an Arduino Uno microcontroller serves as the main control unit, which generates the necessary control signals for the IGBT, thyristors, and FMS. It produces a 980 Hz PWM signal with a duty cycle of 35% during regeneration. In addition, several passive components such as capacitors, inductors, and resistors are employed as breaker and network elements. The experimental setup for the proposed topology is depicted in Figure 12. To extract the presented graphs for experimental results, the data acquisition and control interface (DACI) card (Lab volt 9063) is utilized.

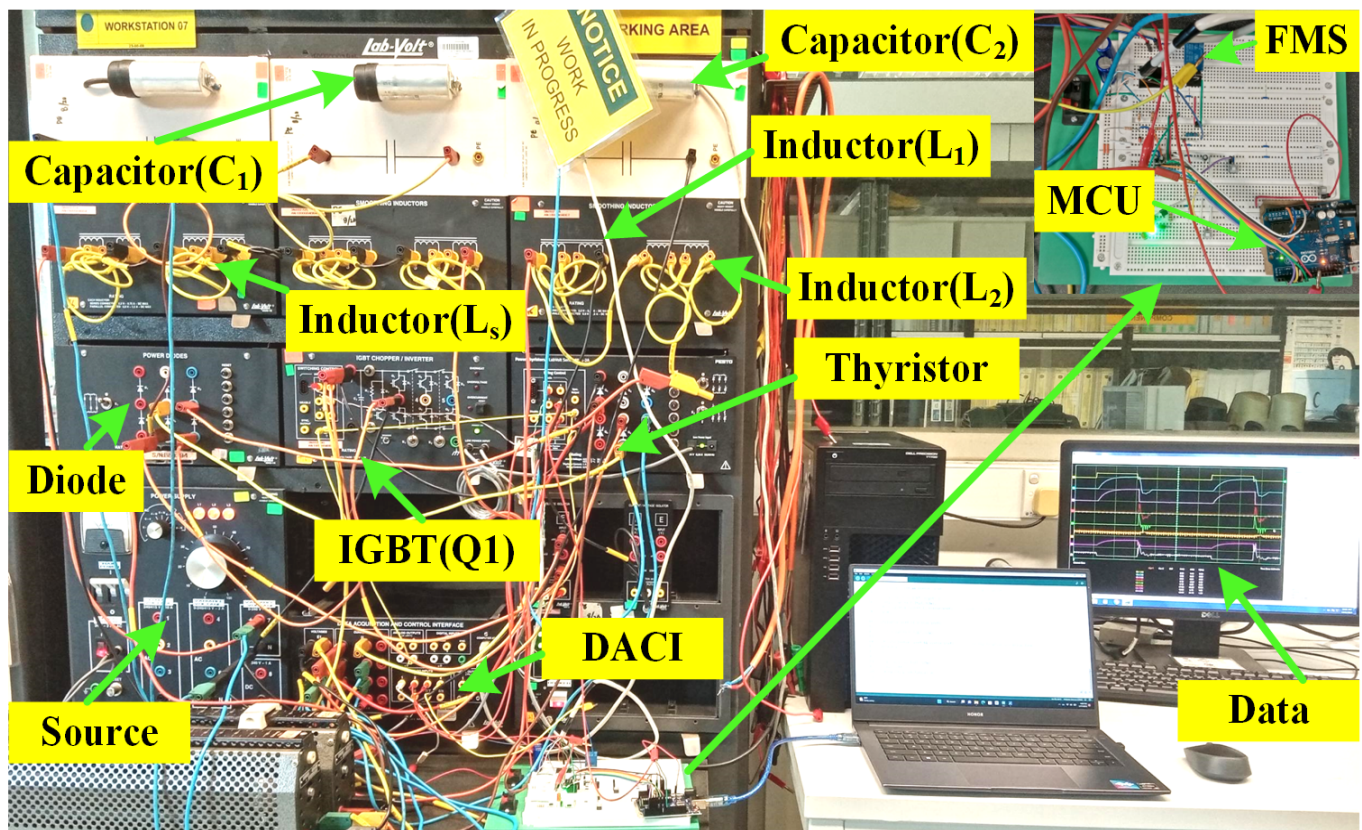


Figure 12. Lab setup of proposed EBDCCB.

4.3.2. Experimental Results

The results obtained from the DACI card using LVDAC-EMS software were exported and subsequently analyzed in MATLAB, as depicted in Figure 13. Figure 13a illustrates the response of the source voltage during breaker turn on, turn off, and the regeneration period. Voltage disturbances occur due to abrupt current breaking and regeneration. The proposed breaker accomplishes current breaking rapidly within 35.16 ms, as demonstrated in Figure 13b. Additionally, this figure displays the regenerated current with a peak of 0.35 A and an average value of 0.24 A. The load voltage and load current, presented in Figure 13c,d, indicate swift isolation of the load from the source. The generated voltage stress across the FMS is 242 V during current interruption, as observed in Figure 13e. To facilitate current breaking and absorb residual energy from the source side inductor, the proposed EBDCCB employs a capacitor (C_1) and an inductor (L_1). The voltage and current responses of the capacitor (C_1) during braking and regeneration are depicted in Figure 13f,g. Furthermore, this EBDCCB utilizes two inductors (L_1 and L_2) for current breaking and regeneration. Figure 13g presents the combined current response through these two inductors, with positive parts representing the current through inductor (L_1) and negative parts representing inductor (L_2), which are separately illustrated in Figure 11b–d. The experiment yielded a regenerated peak power of 30.82 W and an average power of 13.56 W. During current breaking, the total energy supplied by the source side inductor, E_S , was 2.423 J, while the leaked energy to the source, E_{LOAD} , amounted to 0.593 J, which is irrecoverable. The regenerated energy, denoted by E_r , was found to be 1.324 J. By utilizing the formula stated in Equation (26), the energy recovery efficiency was calculated to be 72%. Table 3 provides a summary of the experimental results. With consistent parameters, the simulation was conducted using PSIM. The outcomes revealed remarkable similarity in terms of current breaking time and voltage stress. However, when it comes to current regeneration, the results from both simulations and experimental trials outlined in Table 3 displayed slightly elevated values. This can be attributed to the omission of the internal

resistance of the devices during the analysis. Figure 14 displays the experimental findings pertaining to reverse current breaking. The graph generated exhibits an identical pattern to Figure 13, with the sole distinction being the direction of current owing to the symmetrical nature of the operation and the same network parameters. The synchronized switching pulses of the circuit breaker, in harmony with the source current, are depicted in Figure 15. Upon deactivation of the FMS, the thyristors (T1 and T6) receive a turn-on pulse, initiating the flow of current through the LC network of the breakers. As the source current reaches zero, the controller transmits PWM pulses to the IGBT gates. This leads to the regenerated current redirecting towards the source through thyristor (T2) following the receipt of a turn-on pulse, as illustrated in Figure 15. Figure 14 demonstrates that the results of reverse power flow are symmetrical due to the symmetrical nature of the topology. When the current direction is reversed, it indicates that this breaker can facilitate both reverse power flow and current interruption.

Once the regeneration stage is complete, the circuit breaker will undergo a reset, preparing it for its next operation. The objective of this research is to investigate and develop a DC circuit breaker that provides bidirectional and energy-efficient current interruption while also incorporating energy regeneration. The experimental results obtained in this study provide solid evidence supporting the concepts proposed in this paper. Despite the limitations imposed by the reduced laboratory capacity, the experimental validation of this DCCB primarily focuses on low-voltage scenarios. However, based on the simulation results, it is evident that this DCCB holds significant promise for practical and feasible implementation in high current applications.

Table 3. Experimental results.

Performance Indicators	Experimental	Simulation
Current breaking time (T_{trip})	35.16 ms	34.24 ms
Maximum voltage stress	242 V	239.2 V
Regenerated current (peak)	−0.35 A	−0.47 A
Average regenerated current	−0.24 A	−0.29 A
Regenerated power (peak)	−30.82 W	−38.9 W
Average regenerated power	−13.56 W	−16.49 W
Regenerated energy	1.324 J	1.30 J

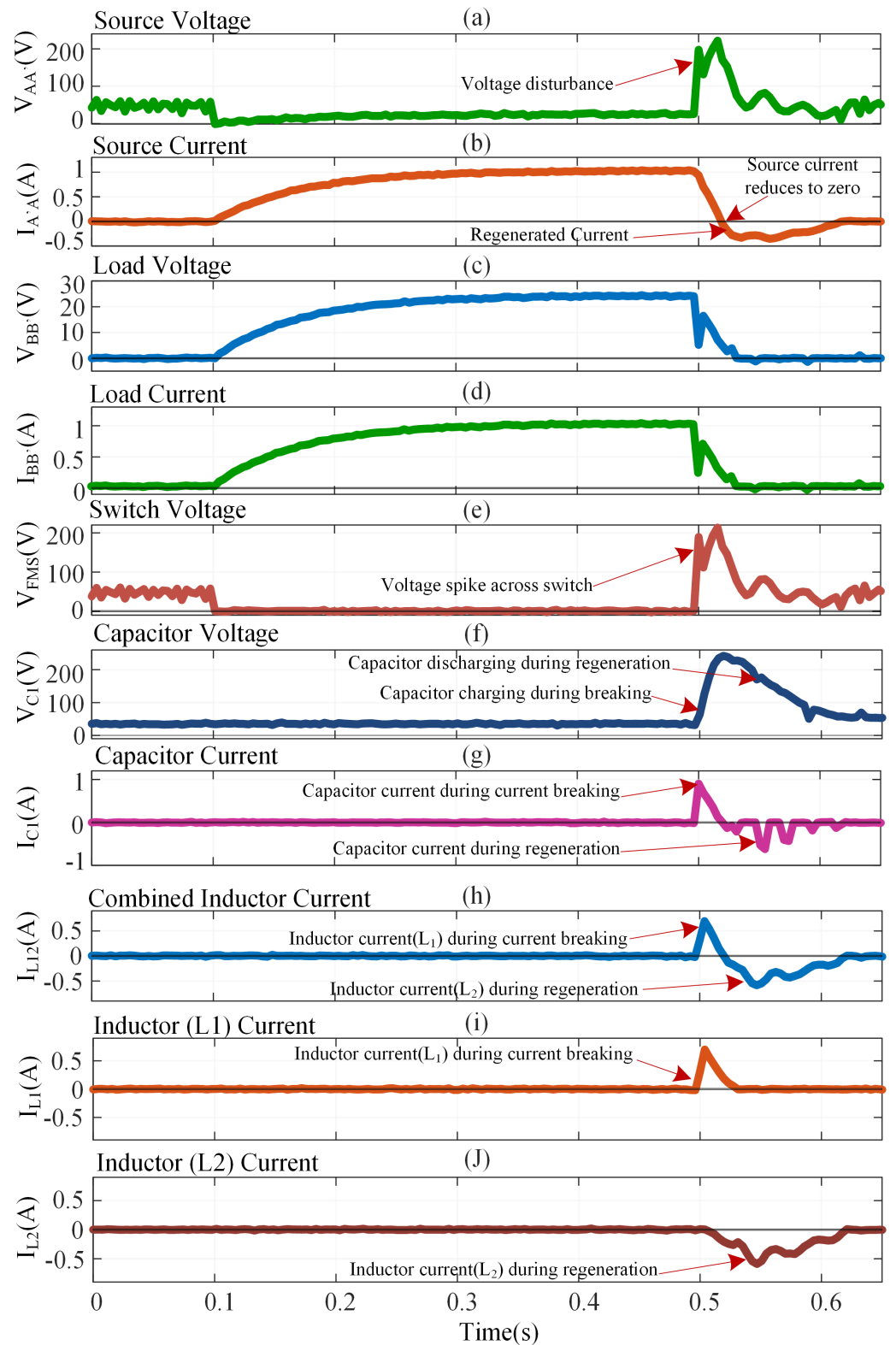


Figure 13. Experimental response of forward power flow for (a) source voltage (b) source current (c) load voltage (d) load current (e) voltage stress across the mechanical switch (f) capacitor voltage (g) capacitor current (h) combined inductor current (i) inductor current during current breaking (j) inductor current during regeneration.

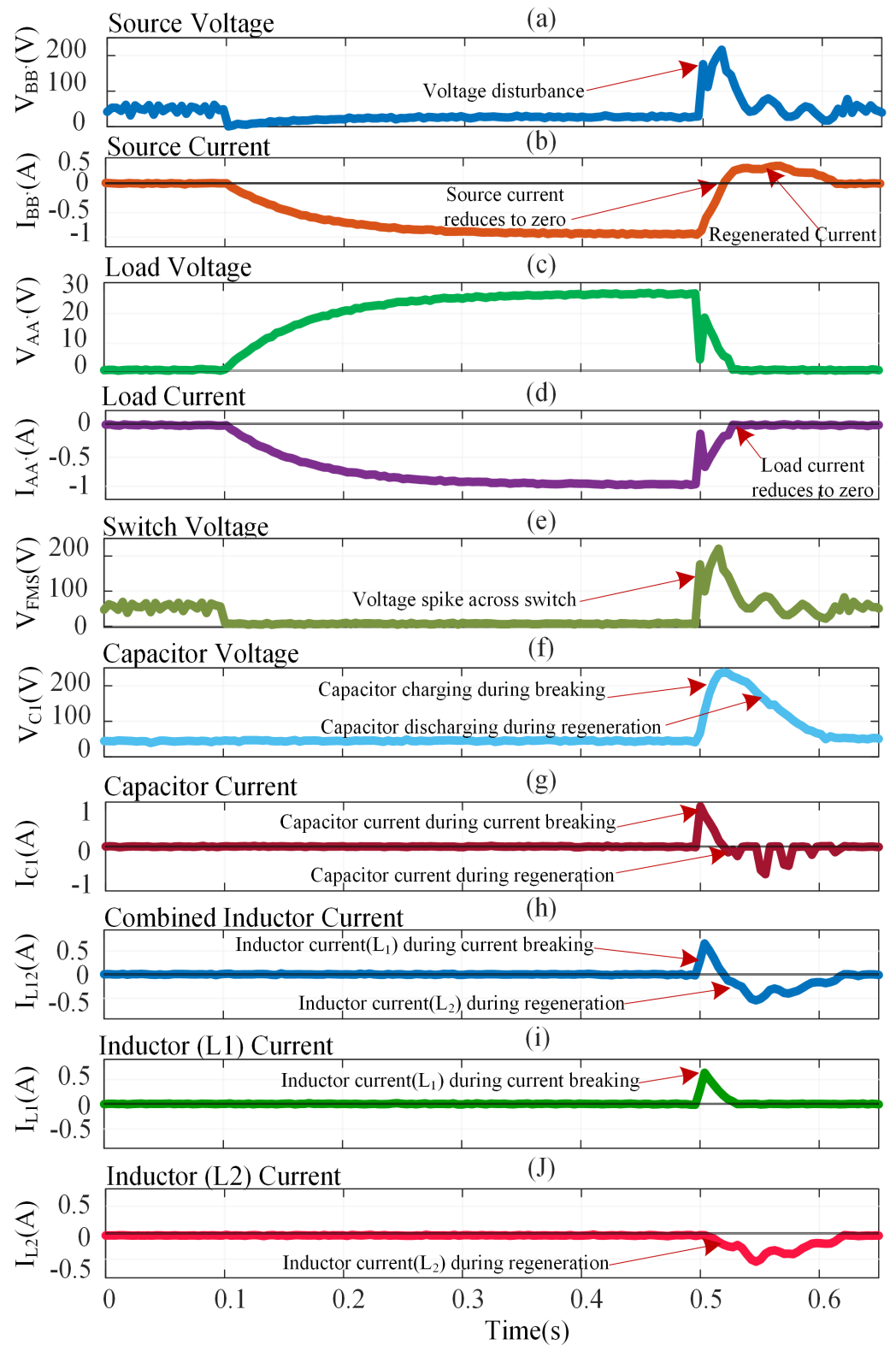


Figure 14. Experimental response of reverse power flow for (a) source voltage (b) source current (c) load voltage (d) load current (e) voltage stress across the mechanical switch (f) capacitor voltage (g) capacitor current (h) combined inductor current (i) inductor current during current breaking (j) inductor current during regeneration.

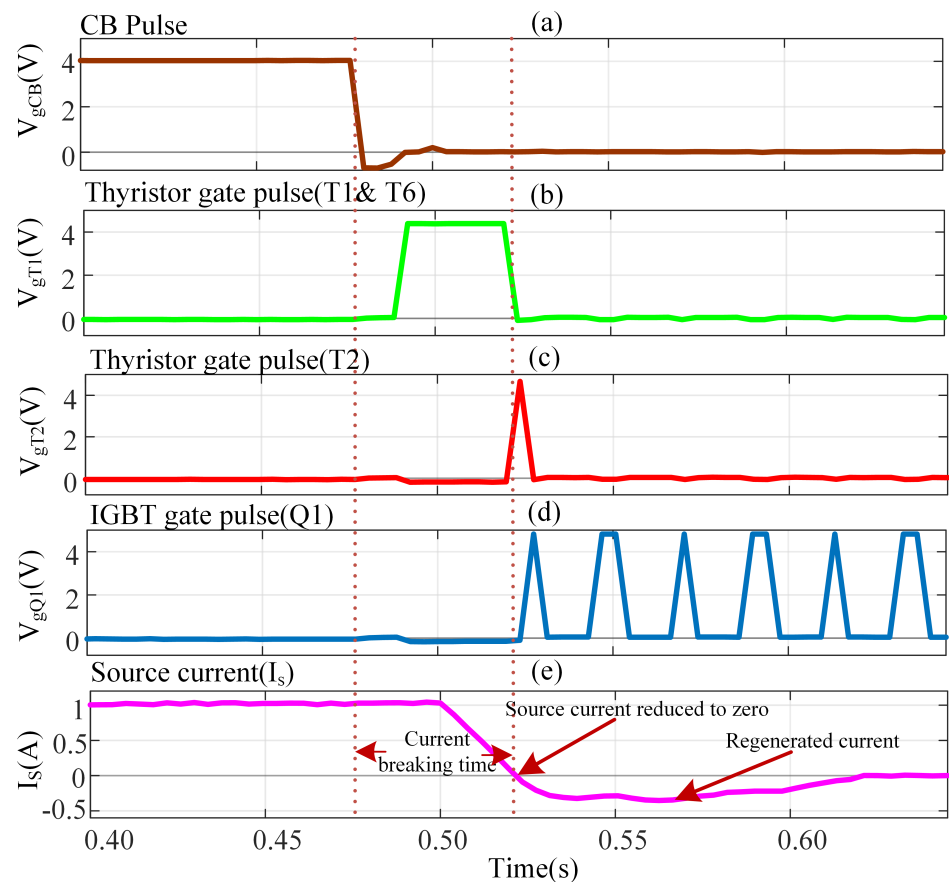


Figure 15. Gate pulses for (a) FMS (b) thyristor (T1, T6) (c) thyristor (T2) (d) IGBT (Q1) (e) source current.

5. Conclusions

The EBDCCB represents a modified version of the hybrid DC circuit breaker, characterized by its ability to harness and reuse the stored energy within the network inductance rather than dissipating it during frequent load switching and fault-clearing intervals. The proposed scheme has undergone thorough validation through extensive simulations conducted using the PSIM software. The results of the simulations have demonstrated notable achievements, including faster current breaking, reduced voltage stress, and a commendable energy recovery rate of 67.27% from the source inductance. Moreover, the proposed scheme has effectively increased the average value of the regenerated current while concurrently reducing the peak value. This reduction is crucial to mitigate voltage disturbances during the regeneration process. Another noteworthy advancement of the modified topology is its bidirectional current-breaking capability, addressing the essential requirement of bidirectional power flow in DC microgrids. The mathematical modeling and experimental results presented in this study provide substantial evidence in support of the proposed topology's effectiveness. Furthermore, a comparative analysis conducted among different DC circuit breaker configurations highlights the significant contributions of this research.

Author Contributions: Conceptualization, M.M.H.; methodology, M.M.H.; software, M.M.H.; validation, M.M.H.; investigation, M.M.H. and R.K.; resources, R.K.; writing—original draft preparation, M.M.H.; writing—review and editing, R.K., S.M.S.L. and L.H.H.; supervision, L.H.H. and R.K.; project administration, L.H.H. All authors have read and agreed to the published version of the manuscript.

Funding: Grant: YUTP 015LC0-485 and graduate assistantship scheme of Universiti Teknologi PETRONAS (UTP), Seri Iskandar, Perak, Malaysia.

Data Availability Statement: Not applicable

Acknowledgments: The authors acknowledge the support from the YUTP 015LC0-485 grant and graduate assistantship scheme for providing financial support. The Department of Electrical and Electronics Engineering, Universiti Teknologi PETRONAS (UTP), Seri Iskandar, Perak, Malaysia provided cutting-edge research facilities.

Conflicts of Interest: The authors declare no conflict of interest.

References

1. Rosli, A. *Malaysia's Extreme Weather Is a Sign That Climate Change Has Arrived on Our Shores*; Juice: Petaling Jaya, Malaysia, 2021.
2. Emanuel, K. Increasing destructiveness of tropical cyclones over the past 30 years. *Nature* **2005**, *436*, 686–688. [[CrossRef](#)]
3. International Energy Agency. Global Energy Review: CO₂ Emissions in 2020. Available online: <https://www.iea.org/articles/global-energy-review-co2-emissions-in-2020> (accessed on 19 August 2022).
4. Yi, L.; Moon, J. Bidirectional QZ-source DC circuit breaker. *IEEE Trans. Power Electron.* **2022**, *37*, 9524–9538. [[CrossRef](#)]
5. Elsayed, A.T.; Mohamed, A.A.; Mohammed, O.A. DC microgrids and distribution systems: An overview. *Electr. Power Syst. Res.* **2015**, *119*, 407–417. [[CrossRef](#)]
6. Beheshtaein, S.; Cuzner, R.; Savaghebi, M.; Guerrero, J.M. Review on microgrids protection. *IET Gener. Transm. Distrib.* **2019**, *13*, 743–759. [[CrossRef](#)]
7. Shutari, H.; Ibrahim, T.; Nor, N.B.; Saad, N.; Tajuddin, M.F.; Abdulrab, H.Q. Development of a Novel Efficient Maximum Power Extraction Technique for Grid-Tied VSWT System. *IEEE Access* **2022**, *10*, 101922–101935. [[CrossRef](#)]
8. Beheshtaein, S.; Cuzner, R.M.; Forouzesh, M.; Savaghebi, M.; Guerrero, J.M. DC microgrid protection: A comprehensive review. *IEEE J. Emerg. Sel. Top. Power Electron.* **2019**. [[CrossRef](#)]
9. Kumar, D.; Zare, F.; Ghosh, A. DC microgrid technology: System architectures, AC grid interfaces, grounding schemes, power quality, communication networks, applications, and standardizations aspects. *IEEE Access* **2017**, *5*, 12230–12256. [[CrossRef](#)]
10. Bini, R.; Backman, M.; Hassanpoor, A. Interruption technologies for HVDC transmission: State-of-art and outlook. In Proceedings of the 2017 4th International Conference on Electric Power Equipment-Switching Technology (ICEPE-ST), Xi'an, China, 22–25 October 2017; pp. 318–323.
11. Ludin, G.A.; Amin, M.A.; Matayoshi, H.; Rangarajan, S.S.; Hemeida, A.M.; Takahashi, H.; Senjyu, T. Solid-state dc circuit breakers and their comparison in modular multilevel converter based-hvdc transmission system. *Electronics* **2021**, *10*, 1204. [[CrossRef](#)]
12. Hassan, M.; Hossain, M.J.; Shah, R. DC fault identification in multiterminal HVDC systems based on reactor voltage gradient. *IEEE Access* **2021**, *18*, 115855–115867. [[CrossRef](#)]
13. Mei, J.; Fan, G.; Ge, R.; Wang, B.; Zhu, P.; Yan, L. Research on coordination and optimal configuration of current limiting devices in HVDC grids. *IEEE Access* **2019**, *7*, 106727–106739. [[CrossRef](#)]
14. Pei, X.; Cwikowski, O.; Vilchis-Rodriguez, D.S.; Barnes, M.; Smith, A.C.; Shuttleworth, R. A review of technologies for MVDC circuit breakers. In Proceedings of the IECON 2016—42nd Annual Conference of the IEEE Industrial Electronics Society, Florence, Italy, 24–27 October 2016; pp. 3799–3805.
15. Xia, N.; Zou, J.; Liang, D.; Gao, Y.; Huang, Z.; Wang, Y. Investigations on the safe stroke of mechanical HVDC vacuum circuit breaker. *J. Eng.* **2019**, *2019*, 3022–3025. [[CrossRef](#)]
16. Abedrabbo, M.; Leterme, W.; Van Hertem, D. Analysis and enhanced topologies of active-resonance DC circuit breaker. In Proceedings of the 2017 19th European Conference on Power Electronics and Applications (EPE'17 ECCE Europe), Warsaw, Poland, 11–14 September 2017; pp. P-1–P-10.
17. Ni, B.; Xiang, W.; Yuan, Z.; Chen, X.; Wen, J. Operation and transient performance of a four-terminal MMC based DC grid implementing high power mechanical DC circuit breaker. *J. Eng.* **2019**, *2019*, 5167–5171. [[CrossRef](#)]
18. Raghavendra, V.; Naik, B.S.; Sreekanth, T.; Chub, A. Controlled bidirectional DC circuit breaker with zero negative current for high load shift applications. *IEEE Trans. Ind. Appl.* **2022**, *58*, 6942–6951. [[CrossRef](#)]
19. Karimi-Ghartemani, M.; Khajehoddin, S.A.; Jain, P.; Bakhshai, A. A systematic approach to DC-bus control design in single-phase grid-connected renewable converters. *IEEE Trans. Power Electron.* **2012**, *28*, 3158–3166. [[CrossRef](#)]
20. Wang, Y.; Li, W.; Wu, X.; Wu, X. A novel bidirectional solid-state circuit breaker for DC microgrid. *IEEE Trans. Ind. Electron.* **2018**, *66*, 5707–5714. [[CrossRef](#)]
21. Kheirollahi, R.; Zhao, S.; Zhang, H.; Lu, F. Fully Soft-Switched DC Solid-State Circuit Breakers. *IEEE Trans. Power Electron.* **2023**, *38*, 6750–6754. [[CrossRef](#)]
22. Ajmal, C.M.; Raghavendra, I.V.; Naik, S.; Ray, A.; Krishnamoorthy, H.S. A modified hybrid DC circuit breaker with reduced arc for low voltage DC grids. *IEEE Access* **2021**, *9*, 132267–132277. [[CrossRef](#)]
23. Liu, L.; Zhuang, J.; Wang, C.; Jiang, Z.; Wu, J.; Chen, B. A hybrid DC vacuum circuit breaker for medium voltage: Principle and first measurements. *IEEE Trans. Power Electron.* **2014**, *30*, 2096–2101. [[CrossRef](#)]
24. Kim, G.; Park, J.H.; Kim, D.Y.; Kim, S.Y.; Kim, T.H.; Jang, H.S.; Lee, Y.W.; Lee, M.J. 4-Pole Hybrid HVDC Circuit Breaker for Pole-to-Pole (PTP) Fault Protection. *IEEE Trans. Power Electron.* **2022**, *10*, 39789–39799. [[CrossRef](#)]

25. Shu, J.; Wang, S.; Ma, J.; Liu, T.; He, Z. An active Z-source DC circuit breaker combined with SCR and IGBT. *IEEE Trans. Power Electron.* **2020**, *35*, 10003–10007. [[CrossRef](#)]
26. Lumen, S.S.; Kannan, R.; Mahmud, M.A.; Yahaya, N.Z. An improved DC circuit breaker topology capable of efficient current breaking and regeneration. *IEEE Trans. Power Electron.* **2021**, *37*, 6927–6938. [[CrossRef](#)]

Disclaimer/Publisher’s Note: The statements, opinions and data contained in all publications are solely those of the individual author(s) and contributor(s) and not of MDPI and/or the editor(s). MDPI and/or the editor(s) disclaim responsibility for any injury to people or property resulting from any ideas, methods, instructions or products referred to in the content.